Plastic Crystal-to-Crystal Transition of Janus Particles under Shear

Zihan Huang, Guolong Zhu, Pengyu Chen, Cuiling Hou, and Li-Tang Yan[*]
State Key Laboratory of Chemical Engineering, Department of Chemical Engineering,
Tsinghua University, Beijing 100084, China

(Received 27 March 2019; published 15 May 2019)

Colloidal Janus spheres in the bulk typically spontaneously assemble into plastic crystalline phases, while particle orientations exhibit glasslike dynamics without long-range order. Through Brownian dynamics simulations, we demonstrate that shear can trigger a phase transition from an isotropic crystal with orientational disorder to an orientationally ordered crystal with lamellae along the shear direction. This nonequilibrium transition is accompanied with the orientational ordering following a nucleation and growth mechanism. By performing a phenomenological extension of free energy analysis, we reveal that the nucleation originates from the orientation fluctuations induced by shear. The growth of the orientationally crystalline cluster is examined to be disklike, captured by developing a lattice model with memoryless state functions. These findings bring new insights into the mechanisms for the ordering transition of anisotropic particles at nonequilibrium states.

DOI: 10.1103/PhysRevLett.122.198002

Concentrated suspensions of colloidal particles are known to undergo self-organization due to the entropy maximization [1–3], leading to a fascinating range of ordered phases at equilibrium states [4–8]. Whereas shape-anisotropic colloids are able to form liquid crystals [7], spherical colloids with surface anisotropy, e.g., Janus spheres [9–13], can assemble into plastic crystals that possess long-range translational order but orientational disorder [14–16]. In particular, free energy calculations [17,18] theoretically confirm that orientational crystals of Janus spheres can be more thermodynamically favored than plastic crystals under certain conditions. However, possibly owing to the kinetic trapping in local free-energy minima, such a prediction has been largely superseded in both experiments and simulations by plastic crystalline phases with slow orientationally glassy dynamics [14]. Nevertheless, the theoretical evidence of orientational crystals gives us confidence in controlling and reconfiguring the orientations of anisotropic particles into ordered states.

In striking contrast to quiescent conditions where systems can readily become kinetically trapped in metastable states, the action of an external stimulus, such as shear flow, can significantly promote the formation of ordered states [19–23]. For instance, by simply increasing the volume fraction beyond the liquid-solid phase transition, crystals of hard spheres tend to be small and predominantly randomly close packed; in comparison, large-area face-centered-cubic (fcc) single crystals can be fabricated when applying a controlled shear to this system [19]. The ability of shear to facilitate crystal formation is significant and well documented [24–27], which can be attributed to the shear-induced enhancement of translational particle diffusion [28]. On the other hand, shear also greatly accelerates particle rotations [29,30], providing a potential approach for systems to escape from orientationally metastable states. However, how to effectively utilize such shear effects to tune the orientational structures of anisotropic particles remains largely unexplored. Whether and how shear can induce orientational ordering of Janus spheres is unclear, leaving an urgent and critical issue to be addressed.

In this Letter, using numerical simulations, we show that shear can trigger a phase transition in a dense suspension of Janus spheres from an initial plastic crystal to an orientational crystal with lamellae along the shear direction. The orientational ordering in this transition follows the nucleation and growth mechanism. A phenomenological extension of free energy analysis is performed to reveal that the nucleation originates from shear-induced orientation fluctuations. The subsequent growth is observed to be disklike, captured by developing a lattice model with memoryless state functions. The findings are of significance in unraveling the mechanisms underlying the phase transition of anisotropic particles at nonequilibrium states, and might suggest extensive applications of reconfigurable materials with tunable orientational orders.

Full technical details on the simulation model are described in the Supplemental Material [31] and briefly introduced here. As shown in Fig. 1(a), the amphipathic character of Janus particles is modeled by an attractive cap (blue) and a repulsive cap (yellow) on the surface. The central half angle α known as the Janus balance [9] characterizes the size of the attractive part. The potential used to model the anisotropic interactions between particles i and j is given by [10]

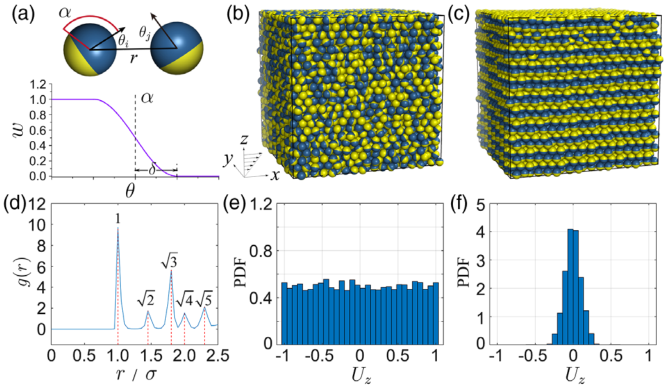

FIG. 1. (a) Schematic diagrams of the Janus-particle model (top) and the angular dependence $w(\theta)$ (bottom). (b) Representative snapshot of the initial state. (c) The snapshot of the shear-induced orientational crystal. (d) Radial distribution function for particle locations in (c). (e)–(f) Probability distributions of U_z for phases in (b) and (c), respectively.

$$U_{ij}(r,\theta_i,\theta_j) = U_{ij}^{\mathrm{rep}}(r) + U_{ij}^{\mathrm{att}}(r,\epsilon)w(\theta_i)w(\theta_j), \quad (1)$$

where r is the distance between two particles, θ_i and θ_j are schemed in Fig. 1(a). $U_{ij}^{\mathrm{rep}}(r)$ is a repulsive interaction and has the form of a truncated Weeks-Chandler-Andersen (WCA) potential. $U_{ij}^{\mathrm{att}}(r,\epsilon)$ with a bond energy ϵ is utilized to describe the short-range attractive interactions between Janus particles. The angular dependence $w(\theta)$ is schematically shown in Fig. 1(a). The natural units for the systems are particle diameter σ, timescale τ and thermal energy k_BT. Bond energy ϵ is set as $7k_BT$, which is close to the experimental value in the works of Chen *et al.* [9,36]. Based on the particle model, we consider a three-dimensional periodic simulation box $L \times L \times L$ ($L = 18.2\sigma$) consisting of $N = 8000$ Janus spheres in the NVT ensemble. Linear shear flow with a shear rate $\dot{\gamma}$ is applied in x direction. The evolution of positions and orientations of Janus particles are simulated by Brownian dynamics [31]. The model validity has been confirmed by reproducing the experimental observations of shear-induced crystallization and melting of colloids (Figs. S1 and S2).

The initial state of the dense suspension of Janus spheres is obtained by sedimentation equilibrium [15], with a representative snapshot shown in Fig. 1(b). Whereas Janus particles exhibit a close-packed structure, particle orientations demonstrate no long-range order, leading to a plastic crystalline phase [17,37]. However, when applying a controlled shear, e.g., $\dot{\gamma} = 0.2\tau^{-1}$, the suspension turns into an orientational-crystal-like phase with lamellae along the shear direction [Fig. 1(c)]. To characterize precisely the structures in this phase, the radial distribution function $g(r)$ for particle locations in Fig. 1(c) is calculated [Fig. 1(d)], indicating a fcc-dominated structure. Moreover, to quantify the orientation distributions, we define a parameter $U_z = \mathrm{sign}(x,y)\|\mathbf{n} \times \mathbf{e}_z\|$ for the orientation vector $\mathbf{n} = (x,y,z)$, where $\mathbf{e}_z = (0,0,1)$. The sign function $\mathrm{sign}(x,y) = 1$ when (i) $x > 0$, and (ii) $x = 0$, $y > 0$. Otherwise $\mathrm{sign}(x,y) = -1$. In Figs. 1(e) and 1(f), we give the distributions of U_z for the snapshots in Figs. 1(b) and 1(c), respectively. In contrast to the uniform distribution in the plastic crystalline phase, the mono-disperse-like U_z in Fig. 1(f) indicates a long-range orientational order. That is, shear-induced phase transition in a dense suspension of Janus spheres is observed, from an initial plastic crystal to an orientational crystal (see also Movie II). For convenience, we use the terms *plastic phase* and *crystalline phase* to denote the phases of plastic crystal and orientational crystal in the following presentations, respectively.

To delineate the shear-induced transition from plastic phases to crystalline phases in more detail, we systematically change the simulation parameters to explore the conditions under which the transition can be observed. Twenty independent runs are performed for each parameter set. To quantify the global orientational order of system, order parameter $\langle P_2\rangle$ [38,39] is used and defined as below. For the ith Janus particle with an orientation vector $\mathbf{n}_i$, the local order parameter is given by

$$P_2(i) = \frac{3}{2N_b(i)}\sum_{j=1}^{N_b(i)}(\mathbf{n}_i\cdot\mathbf{n}_j)^2 - \frac{1}{2}, \quad (2)$$

where $N_b(i)$ is the number of near neighbors of particle i lying within the potential cutoff. $\langle P_2\rangle$ is obtained by the average of $P_2(i)$ over all particles in the system.

First, the influences of Janus balance are considered. Time evolutions of $\langle P_2\rangle$ for systems under shear ($\dot{\gamma} = 0.2\tau^{-1}$) with various α are shown in Fig. 2(a). It can be found that high values of $\langle P_2\rangle$ locate at the regions where α ranges nearly from 100° to 120°, suggesting that shear-induced orientational crystals are only accessible for

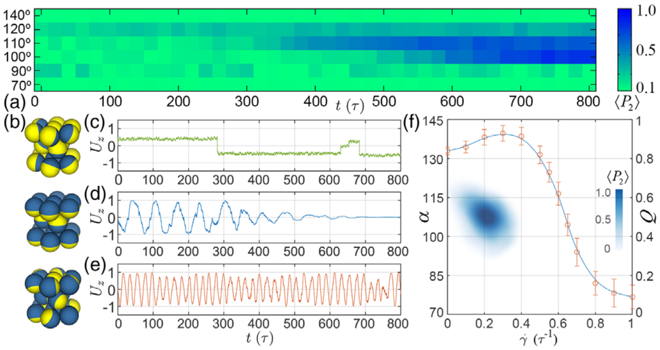

FIG. 2. (a) Time evolutions of $\langle P_2\rangle$ for systems with various α at $\dot{\gamma} = 0.2\tau^{-1}$. (b) Representative local structures of systems under shear where $\alpha = 65°$ (top), 105° (middle), and 150° (bottom), respectively. (c)–(e) Time dependences of U_z for a single particle with $\alpha = 105°$ under shear, where $\dot{\gamma} = 0$ (c), $0.2\tau^{-1}$ (d), and $0.6\tau^{-1}$ (e), respectively. (f) Left: heatmap of $\langle P_2\rangle$ on the $\dot{\gamma}-\alpha$ space. Right: the plot of Q vs $\dot{\gamma}$.

those Janus balances. To rationalize this intuitively, we show the representative local structures of systems under shear with $\alpha = 65°$, $105°$, and $150°$ in Fig. 2(b). For small α, the weak bonding abilities of Janus particles are unable to maintain the lamellae along the shear direction. Instead, tetrahedra phases are more preferred owing to their bonding stability. For large α, the size of the attractive cap is close to the limit of full coverage, leading to an isotropiclike potential, which results in a uniform distribution of particle orientations.

Next, we turn to the effects of shear strength by systematically changing $\dot{\gamma}$. As shown in Figs. 2(c)–2(e), typical time dependences of U_z for a single particle demonstrate that the rotational dynamics of Janus particles under various shear rates can be completely different. At equilibrium states where $\dot{\gamma} = 0$, discrete and large angular jumps of U_z are occasionally observed [Fig. 2(c)], suggesting an orientationally glassy dynamics (Fig. S3) [14]. For $\dot{\gamma} = 0.2\tau^{-1}$ at which the orientational ordering occurs, the rotation of a Janus particle is gradually suppressed and finally freezes with the orientation along the z direction [Fig. 2(d)]. For high shear rates like $\dot{\gamma} = 0.6\tau^{-1}$, the oscillatory evolution of U_z indicates that the Janus particle undergoes a periodic tumbling motion [Fig. 2(e)]. For a legible presentation of shear effects on the global orientational order, the heatmap of $\langle P_2 \rangle$ on the $\dot{\gamma} - \alpha$ space is plotted in Fig. 2(f). In particular, high values of $\langle P_2 \rangle$ emerge only for $\dot{\gamma} < 0.4\tau^{-1}$. One reason is the shear-induced tumbling of particles under a strong shear [Fig. 2(e)], resulting in the melting of particle orientations. Another is the collapse of crystalline structures under a high shear rate, which is characterized by the decrease of crystallinity Q [40,41] (defined in the Supplemental Material [31]) for $\dot{\gamma} > 0.4\tau^{-1}$ [Fig. 2(f)].

To pinpoint the mechanisms of shear-induced orientational ordering, we perform a phenomenological extension of free energy analysis. It is reasonable to expect that for moderate shear rates the system can be approximately captured by a thermodynamic description [28,42]. Under this assumption, a modified Helmholtz free energy per particle can be given by [31]

$$f = \langle U \rangle - T\langle S \rangle. \tag{3}$$

Here $\langle U \rangle$ and $\langle S \rangle$ are the ensemble averages of pair potentials and orientational entropy respectively. Detailed calculations of $\langle U \rangle$ and $\langle S \rangle$ are given in the Supplemental Material [31]. In Fig. 3(a), we show the Janus-balance dependences of f for both the plastic phase (f_p) and crystalline phase (f_c), where f_p exceeds f_c when α ranges nearly from 90° to 127° (denoted as critical Janus balances). This result suggests that the crystalline phase is more thermodynamically stable than the plastic one for those α, which is consistent with the observations shown in Fig. 2(f). Generally, we calculate the critical Janus balances for different ϵ and show the phase diagram on the $\epsilon - \alpha$ space in Fig. 3(b). The systems where a relatively long-range orientational order can be observed ($\langle P_2 \rangle > 0.5$, blue crosses) all locate in the crystalline-phase regime. That is, the orientational ordering occurs only when the condition is thermodynamically favored for crystalline phases. Therefore, in the free-energy landscape, orientational ordering is a transition in which a system in the metastable plastic phase escapes to the stable crystalline phase under the disturbance exerted by shear.

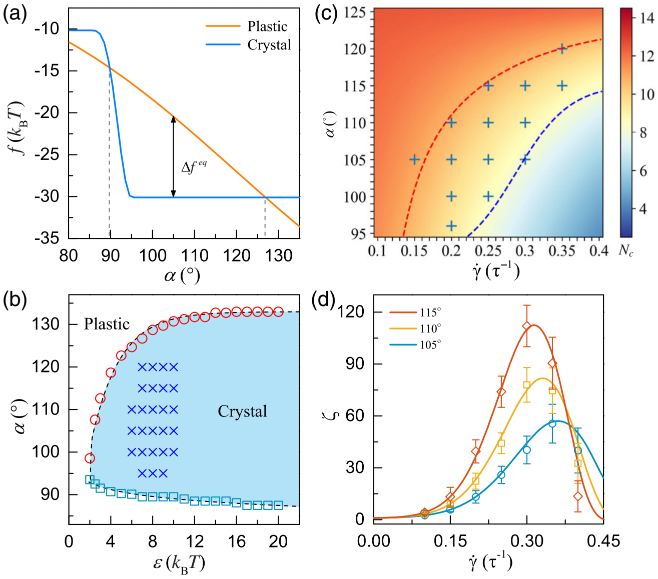

FIG. 3. (a) f for both plastic and crystalline phases when $\epsilon = 7k_BT$. The double sided arrow denotes the definition of Δf^{eq}. (b) Phase diagram on the $\epsilon - \alpha$ space. (c) Heatmap of N_c on the $\dot{\gamma} - \alpha$ space predicted by Eq. (4). The blue and red dashed lines are the contour lines for $N_c = 8$ and 11, respectively. The blue crosses in (b) and (c) represent the systems where $\langle P_2 \rangle > 0.5$. (d) The shear-rate dependence of ζ for $\alpha = 105°$, 110°, and 115° respectively. The solid lines are theoretical predictions obtained by Eq. (5).

Based on this principle, we turn to the transition kinetics of the orientational ordering. Time evolution of U_z in Fig. 2(d) indicates that the initial orientation of a Janus particle is first reconfigured by shear. Such reconfigurations significantly enhance the fluctuations of particle orientations, allowing more opportunities for the emergence of a stable orientational nucleus. A nucleus can form when the size of a randomly formed metastable precursor reaches the threshold N_c [43]. An extension of the classic nucleation theory gives the criterion for N_c, expressed as [31]

$$\frac{\sqrt[3]{18\pi}}{\sqrt[3]{N_c}} - \frac{4}{\sqrt{3N_c}} = c_{bi}\dot{\gamma}^2 \Delta f^{eq} + 1, \tag{4}$$

where $\Delta f^{eq} = f_c - f_p$, as schemed in Fig. 3(a). c_{bi} is a factor depending on ϵ, and is about $-0.15\tau^2 (k_BT)^{-1}$ when $\epsilon = 7k_BT$. We plot the heatmap of N_c predicted by Eq. (4)

on the $\dot{\gamma} - \alpha$ space in Fig. 3(c). Systems where $\langle P_2 \rangle > 0.5$ (blue crosses) mainly locate in the regime where N_c ranges from 8 to 11 [blue and red dashed lines in Fig. 3(c)], indicating that the nucleus is stable when comprising of 8–11 oriented Janus particles. Based on this criterion, the shear effects on the nucleation rate are investigated. We identify a nucleus using the method described in Ref. [22], and use the reciprocal of the averaged formation time as the nucleation rate. As shown in Fig. 3(d), the rescaled nucleation rate ζ [31] increases with $\dot{\gamma}$ for small shear rates and sharply decreases when shear becomes strong. To rationalize this observation, we propose a theoretical justification based on the assumption that fluctuations of particle orientations induce the formation of a nucleus, given by [31]

$$\zeta = \prod_{i=1}^{N_c/2} (1 + a\dot{\gamma}^2)(1 - b\dot{\gamma}^2). \tag{5}$$

Here, N_c is set as 8, and a, b are factors determined by solving a nonlinear least squares problem [31]. The high agreement between simulation results and predictions of Eq. (5) [Fig. 3(d)] suggests that the nucleation originates from the shear-induced orientation fluctuations.

The nucleation subsequently enables the growth of an orientational crystal. To quantify the growth process, we use the criterion $|U_z| < 0.2$, lasting for at least 1τ, to identify whether the ith Janus particle is oriented. We show the typical snapshots of the system with $\alpha = 105°$ and $\dot{\gamma} = 0.2\tau^{-1}$ at different times in Fig. 4(a), where only the oriented particles are plotted. It can be found that the cluster of oriented particles is oblate and demonstrate a disklike growth perpendicular to the shear direction. For a statistical presentation of such growth way, we divide the simulation box into $L_c \times L_c \times L_c$ cells ($L_c = 11$ in this Letter) and calculate the relative number density $\hat{\rho} = L_c^3 \hat{N}_c / N$ for each cell, where $\hat{N}_c$ is the number of oriented particles in that cell. The mean values of $\hat{\rho}$ along the y axis are calculated and displayed in a heatmap on the xz plane, as schemed in Fig. 4(b). We use the ensemble average of $\hat{\rho}$ based on 10 independent runs, and show the evolution of $\hat{\rho}$ in Fig. 4(c). The value of $\hat{\rho}$ increases oblately along the z direction over time, corroborating statistically that the growth of an orientationally crystalline cluster is disklike.

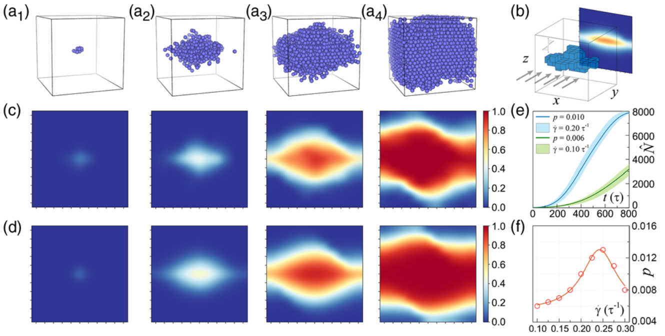

FIG. 4. (a) Representative snapshots of the system with $\alpha = 105°$ and $\dot{\gamma} = 0.2\tau^{-1}$ at $t = 10\tau$ (a$_1$), 200τ (a$_2$), 400τ (a$_3$), and 600τ (a$_4$) respectively. (b) Schematic diagram of calculating the heatmap of $\hat{\rho}$ on the xz plane. (c) The heatmaps of $\hat{\rho}$ in simulations. (d) The heatmaps of $\hat{\rho}$ reproduced by the lattice model. Times of snapshots in (c) and (d) are the same with those in (a). (e) Time dependences of $\hat{N}$ for $p = 0.006$ and 0.010 (lattice model). The confidence intervals of $\hat{N}$ in simulations for $\dot{\gamma} = 0.10$ and $0.20\tau^{-1}$ ($\alpha = 105°$) are also given. (f) The plot of p vs $\dot{\gamma}$ when $\alpha = 105°$.

To reveal the underlying mechanisms of this disklike growth, we develop a lattice model with memoryless state functions to reproduce the time evolution of $\hat{\rho}$. Full details of the lattice model are provided in the Supplemental Material (Fig. S4) [31] and briefly summarized here. For the $L_c \times L_c \times L_c$ cells mentioned above, the coordinate of the ith cell is set as $\mathbf{r}_i = (x, y, z)$ where x, y, and z are integers from $-(L_c - 1)/2$ to $(L_c - 1)/2$. To characterize the state of particle orientations, an oriented state function $\mathcal{S}(\mathbf{r}_i)$ of the ith cell is defined as follows: $\mathcal{S}(\mathbf{r}_i) = 1$ when the particles in the cell are all oriented and $\mathcal{S}(\mathbf{r}_i) = 0$ otherwise. At the beginning, $\mathcal{S}$ for all cells are set as 0 except for the cell at origin $\mathbf{r} = (0, 0, 0)$, representing the stable nucleus. To describe the growth in the model, the ith cell with $\mathcal{S}(\mathbf{r}_i) = 0$ has two approaches to transform into $\mathcal{S}(\mathbf{r}_i) = 1$ at each step, i.e., growing in the horizontal directions (x and y) with a probability p_h and vertical (z) with a probability p_v, respectively. We assume that the growth process is memoryless; i.e., the probabilities at step t depend only on the surrounding state attained in the previous step $t - 1$. Under this assumption, p_h and p_v take form as [31]

$$p_{h,t}(\mathbf{r}_i) = p(\dot{\gamma}, \alpha) \times \sum_{k=1}^{4} \mathcal{N}_{t-1}(\mathbf{r}_i, k), \tag{6}$$

$$p_{v,t}(\mathbf{r}_i) = p(\dot{\gamma}, \alpha) \times \mathcal{L}_{t-1}(\mathbf{r}_i). \tag{7}$$

Here, $p(\dot{\gamma}, \alpha)$ is the intrinsic probability determining the growth rate. $\mathcal{N}_t(\mathbf{r}_i, k) (k = 1, 2, \ldots, 6)$ are the states of six adjacent cells surrounding the ith cell. $\mathcal{L}_t$ describes the shear effects in the vertical direction, which decreases the growth rate when shear-induced displacement is nontrivial. The explicit definitions of $\mathcal{N}_t$ and $\mathcal{L}_t$ are given in the Supplemental Material [31]. To model the shear flow in x direction, state functions are updated at each step by $\mathcal{S}[(x, y, z)] \leftarrow \mathcal{S}[\mathcal{P}(x - z, y, z)]$, where $\mathcal{P}(\mathbf{r})$ represents the coordinate transformed by periodic boundary conditions.

As shown in Fig. 4(d), by choosing an appropriate value of $p(\dot{\gamma}, \alpha)$, the evolution of $\hat{\rho}$ can be effectively reproduced, which also demonstrates a clear emergence of disklike growth (Fig. S5). To quantitatively examine whether the lattice model can capture the growth of a crystalline cluster, we compare the cluster size in simulations with the predicted one $\hat{N} = N\sum_{i=1}^{L_c^3}\mathcal{S}(\mathbf{r}_i)/L_c^3$ in the lattice model. Through the ensemble average, it can be found that simulation results at $\dot{\gamma} = 0.10$ and $0.20\tau^{-1}$ highly agree with model predictions at $p = 0.006$ and 0.010, respectively [Fig. 4(e)], indicating that the cluster growth can be rationalized by the lattice model. Consequently, the relation between $p(\dot{\gamma}, \alpha)$ and $\dot{\gamma}$ is further examined and shown in Fig. 4(f). Similar with the nucleation rate, p increases with $\dot{\gamma}$ for small shear rates, and undergoes an abrupt decrease when shear is strong. That is, the delicate interplay between the nucleation rate and growth rate gives rise to the shear-rate dependence of the orientational ordering ($\langle P_2\rangle$) shown in Fig. 2(f).

In summary, using Brownian dynamics simulations, we demonstrate a novel phase transition in a dense suspension of Janus spheres under shear, from an initial plastic crystal to an orientational crystal with lamellae along the shear direction. The orientational ordering in the transition follows the nucleation and growth mechanism. By performing a phenomenological extension of free energy analysis, we reveal that the nucleation originates from shear-induced orientation fluctuations. The subsequent growth of the orientationally crystalline cluster is examined to be disk-like, captured by developing a lattice model with memoryless state functions. To the best of our knowledge, this is the first demonstration of shear-induced orientational crystallization for dense anisotropic particles. Our results indicate that the combination of anisotropy and shear is important for shedding light on the fundamental physics underlying phase transitions as well as for guiding the design of reconfigurable materials towards desired properties.

We thank Xinghua Zhang and Bing Liu for helpful discussions. We acknowledge financial support from National Natural Science Foundation of China (Grants No. 21873053 and No. 51633003). L.-T. Y. acknowledges financial support from Ministry of Science and Technology of China (Grant No. 2016YFA0202500).

---

[*] ltyan@mail.tsinghua.edu.cn

[1] D. Frenkel, Nat. Mater. **14**, 9 (2015).
[2] U. Agarwal and F. A. Escobedo, Nat. Mater. **10**, 230 (2011).
[3] M. Engel, P. F. Damasceno, C. L. Phillips, and S. C. Glotzer, Nat. Mater. **14**, 109 (2015).
[4] W. K. Kegel, Langmuir **16**, 939 (2000).
[5] E. Zaccarelli, C. Valeriani, E. Sanz, W. C. K. Poon, M. E. Cates, and P. N. Pusey, Phys. Rev. Lett. **103**, 135704 (2009).
[6] B. de Nijs, S. Dussi, F. Smallenburg, J. D. Meeldijk, D. J. Groenendijk, L. Filion, A. Imhof, A. van Blaaderen, and M. Dijkstra, Nat. Mater. **14**, 56 (2015).
[7] L. Onsager, Ann. N.Y. Acad. Sci. **51**, 627 (1949).
[8] G. van Anders, D. Klotsa, N. K. Ahmed, M. Engel, and S. C. Glotzer, Proc. Natl. Acad. Sci. U.S.A. **111**, E4812 (2014).
[9] Q. Chen, J. K. Whitmer, S. Jiang, S. C. Bae, E. Luijten, and S. Granick, Science **331**, 199 (2011).
[10] W. L. Miller and A. Cacciuto, Phys. Rev. E **80**, 021404 (2009).
[11] F. Sciortino, A. Giacometti, and G. Pastore, Phys. Rev. Lett. **103**, 237801 (2009).
[12] T. Vissers, Z. Preisler, F. Smallenburg, M. Dijkstra, and F. Sciortino, J. Chem. Phys. **138**, 164505 (2013).
[13] Y. Iwashita and Y. Kimura, Soft Matter **10**, 7170 (2014).
[14] S. Jiang, J. Yan, J. K. Whitmer, S. M. Anthony, E. Luijten, and S. Granick, Phys. Rev. Lett. **112**, 218301 (2014).
[15] D. J. Beltran-Villegas, B. A. Schultz, N. H. P. Nguyen, S. C. Glotzer, and R. G. Larson, Soft Matter **10**, 4593 (2014).
[16] H. Rezvantalab, D. J. Beltran-Villegas, and R. G. Larson, Phys. Rev. Lett. **117**, 128001 (2016).
[17] H. Shin and K. S. Schweizer, Soft Matter **10**, 262 (2014).
[18] F. Sciortino, A. Giacometti, and G. Pastore, Phys. Chem. Chem. Phys. **12**, 11869 (2010).
[19] R. M. Amos, J. G. Rarity, P. R. Tapster, T. J. Shepherd, and S. C. Kitson, Phys. Rev. E **61**, 2929 (2000).
[20] J. Vermant and M. J. Solomon, J. Phys. Condens. Matter **17**, R187 (2005).
[21] Y. L. Wu, D. Derks, A. van Blaaderen, and A. Imhof, Proc. Natl. Acad. Sci. U.S.A. **106**, 10564 (2009).
[22] R. A. DeLaCruz-Araujo, D. J. Beltran-Villegas, R. G. Larson, and U. M. Córdova-Figueroa, Langmuir **34**, 1051 (2018).
[23] J. Ruiz-Franco, J. Marakis, N. Gnan, J. Kohlbrecher, M. Gauthier, M. P. Lettinga, D. Vlassopoulos, and E. Zaccarelli, Phys. Rev. Lett. **120**, 078003 (2018).
[24] T. M. Slawecki, C. J. Glinka, and B. Hammouda, Phys. Rev. E **58**, R4084 (1998).
[25] J. Jiang, C. Burger, C. Li, J. Li, M. Y. Lin, R. H. Colby, M. H. Rafailovich, and J. C. Sokolov, Macromolecules **40**, 4016 (2007).
[26] A. Nikoubashman, G. Kahl, and C. N. Likos, Soft Matter **8**, 4121 (2012).
[27] S. Sarman, Y.-L. Wang, and A. Laaksonen, Phys. Chem. Chem. Phys. **21**, 292 (2019).
[28] D. Richard and T. Speck, Sci. Rep. **5**, 14610 (2015).
[29] E. Bianchi, A. Z. Panagiotopoulos, and A. Nikoubashman, Soft Matter **11**, 3767 (2015).
[30] Z. Huang, P. Chen, Y. Yang, and L.-T. Yan, J. Phys. Chem. Lett. **7**, 1966 (2016).
[31] See Supplemental Material at http://link.aps.org/supplemental/10.1103/PhysRevLett.122.198002 for computational details, validations of simulation model, the details of free energy analysis and lattice model, as well as two movies, which includes Refs. [32–35].
[32] J. Kim, C. Kim, and B. J. Sung, Phys. Rev. Lett. **110**, 047801 (2013).
[33] C. Greco and A. Ferrarini, Phys. Rev. Lett. **115**, 147801 (2015).
[34] N. J. Terrill, P. A. Fairclough, E. Towns-Andrews, B. U. Komanschek, R. J. Young, and A. J. Ryan, Polymer **39**, 2381 (1998).
[35] R. Li, Y. Wu, and J. Xiao, J. Chem. Phys. **140**, 034503 (2014).
[36] X. Mao, Q. Chen, and S. Granick, Nat. Mater. **12**, 217 (2013).

[37] B. Liu, T. H. Besseling, A. van Blaaderen, and A. Imhof, Phys. Rev. Lett. **115**, 078301 (2015).

[38] P. R. ten Wolde, M. J. Ruiz-Montero, and D. Frenkel, J. Chem. Phys. **104**, 9932 (1996).

[39] A. Cuetos and M. Dijkstra, Phys. Rev. Lett. **98**, 095701 (2007).

[40] W. Lechner and C. Dellago, J. Chem. Phys. **129**, 114707 (2008).

[41] H. Eslami, P. Sedaghat, and F. Müller-Plathe, Phys. Chem. Chem. Phys. **20**, 27059 (2018).

[42] R. Blaak, S. Auer, D. Frenkel, and H. Löwen, Phys. Rev. Lett. **93**, 068303 (2004).

[43] Z. Wang, F. Wang, Y. Peng, Z. Zheng, and Y. Han, Science **338**, 87 (2012).